Parameters and their impacts on the temperature distribution and thermal gradient of solid oxide fuel cell

Erdogan Guk[a,b], Vijay Venkatesan[a], Shumaila Babar[a], Lisa Jackson[a], Jung-Sik Kim[a,*]

[a] Aeronautical & Automotive Engineering Department, Loughborough University, LE11 3TU, United Kingdom
[b] Bozok Üniversitesi, Mühendislik-Mimarlık Fakültesi, Erdoğan AKDAĞ Kampüsü, Atatürk Yolu 7. km, Yozgat, Turkey

HIGHLIGHTS

- Individual parameter contributions to the thermal gradient were revealed.
- Numeral analysis performed to validate experimental findings.
- Gas leakage was the most dominant contributor to temperature rise.
- Electrochemical reaction was the most dominant contributor to thermal gradient.
- Thermal plot of cell area used as tool for determining heat source.

ARTICLE INFO

ABSTRACT

The commercialisation potential of Solid Oxide Fuel Cell is hindered due to certain technical issues. One of these is the thermal gradient across the cell structure during its operational period that can deteriorate the system's performance. In this study, a newly developed *multi-point thermal sensor* is deployed across the cathode to understand the impact of various factors including cell's operating temperature, fuel flow rate and drawing current density on temperature distribution and its stability. Here we report that direct oxidation of hydrogen due to fuel crossover has been the most impactful contributor for the cell's average temperature increment during both open circuit voltage and loading conditions, while electrochemical oxidation of hydrogen is the most impactful contributor for cell temperature gradient during loading. A relationship has been established between the temperature profile of the cell surface and the source of the temperature variation which allows identification of the responsible parameter.

1. Introduction

SOFCs have huge potential for a diverse range of applications. They have the highest operating temperature (600–1000 °C) amongst fuel cells [1–3]. Due to their high operating temperature, they have the flexibility to utilise a variety of fuels including hydrocarbons (such as methane (CH_4)), poisons such as carbon monoxide (CO), as well as biogas mixtures (e.g. syngas) without requiring expensive novel catalyst materials [4]. Its efficiency can reach up to 70% by combining with other energy generating systems which require heat to operate, such as gas turbines [5]. SOFCs have been used in stationary power and auxiliary applications as power sources [6–8]. Its development has sustained growing interest for researchers and companies alike, such as Bloom Energy, DELPHI, FuelCell Energy, Protonex (USA), Catator (Sweden), Ceres power (UK), SOFCMAN (China), MHI (Japan) [9].

Extensive research has been carried out on cell structure, size, layout, fuel suitability etc. to obtain optimum output. However, there are recurring performance degradation issues due to high operating temperature, presenting major obstacles towards SOFC technology to be fully commercialised [6,10,11]. The high temperature-correlated degradation mechanisms (often leading to material deformation) are among the primary contributors for performance degradation of SOFCs [1,3,10,12–14].

Thus, understanding the temperature distribution within SOFCs during operation is vital for effective health management. For instance, thermal stress, as a hard failure, is induced by the high operating temperature and thermal gradient across the cell due to different coefficients of thermal expansion (CTEs) of the cell components, leading to micro-scale cell component cracking and sealing-related problems, and eventually resulting in performance degradation or

system failure [15]. Numerous efforts have been conducted including deep learning [16] and numerical modelling, to predict the temperature distribution of the SOFCs; in contrast, only a limited number of experimental works are available in the literature [17–19].

The numerical studies aid in identifying key factors including current density and flow configuration as the main contributors to the temperature distribution of SOFCs, as well as uneven-temperature-induced thermal stresses and fault diagnosis. Additionally, numerical analysis is required to validate the experimentally-obtained data without the cost or duration of repeated experiments [20]. However, Schlegl and Dawson [20] also emphasize the importance of the experimental validation of the results obtained from numerical analysis. This arises from the difficulty in possessing reliable inputs including Young's modulus, Poisson's ratio, and the thermal expansion coefficient that can vary depending on the fabrication process for the numerical analysis. Aydin, Nakajima, and Kitahara [21] claim that further validations of the reliability of numerical studies based on conventional I–V (current-voltage) curve are required. This is because some average values are used as the main parameters for investigating the relationship between temperature variation and current. Therefore, the validation of the parametric numerical studies with experimentally-obtained data has vital importance, underlining the need for experimental measurement of SOFC temperature distribution.

It is clearly understood that the overall oxidation reaction is exothermic and that released heat, together with electrical power and product gas species, are the reaction by-products [22,23,18,24]. The uniformity of the released heat along the electrode surface is a key parameter in ensuring minimal thermal gradient across the cell surface and the uneven-temperature-induced thermal stresses. The impact of the fuel flow direction or its dilution [25], thermal cycling [26], and uneven material composition on the thermal gradient of SOFCs have been examined and cited as the main contributors to the thermal gradient issue [27–29,25,30]. The impact of the current collection on cell performance has been the main focus in many studies [31–34], rather than establishing the relationship between the temperature gradient and the current collection mechanism.

In the presented work, the individual effect of parameters such as operating temperature, fuel flow rate and electrochemical activity on both temperature average increment (CTA) and cell temperature gradient (CTG) is investigated with *in-situ thermal sensors* (developed in-house) [35,36]. The sensor array's sixteen sensing points (SSPs) are mounted on the cathode surface. In addition, the sensor readings are analysed in conjunction with readings from commercial K-type thermocouples (located 2 mm away from the cathode) to compare their respective temporal and spatial resolutions. For a given set of parameters, once the performance is stabilised and the system reaches a reasonable equilibrium, the corresponding analytical temperature rise is calculated and compared with the experimentally obtained increment. In the current study, individual contributions of parameters such as operating temperature, fuel/air flow rate, and the loading rate are analysed. The importance of quantifying the effect and weight of the individual contributions to the observed temperature gradient in the working SOFC is the main objective. Commercial thermocouples are also employed at the cathode surface to record the time-dependent response of the temperature variation with the corresponding parameters such as flow rate or loading rate. The intent and impetus behind the conception of the sensors was to provide a spatial and temporal in-situ view of the cell temperature, and utilise thin-film/micro-scale techniques tool to provide an insight to the cell behaviour. In the longer term, it could allow validation of numerical studies for the analysis of the materials and mechanistic phenomena of energy devices such as fuel cells and batteries throughout their in-operando thermal monitoring with high resolution [37], as well as provide inputs and training for fault detection using methods such as deep learning.

2. Method

2.1. Materials

Commercially available anode-supported planar SOFC (FuelCellStore, US) is used for the experiment. The cell is comprised of 500–600 μm thick Ni-YSZ (yttria stabilized zirconia) anode, 10 μm YSZ electrolyte, 5 μm GDC (gadolinium doped ceria) barrier layer, and 50 μm LSCF cathode. The cell is placed in an in-house designed Macor™ manifold by sandwiching two gaskets (Thermiculite® 866). Silver wires are used for electrical connections for both anode and cathode sides. K-type commercial thermocouples are used in this study. To make measurements comparable, the *thermal sensor* is made with the same type of thermoelements (i.e. Alumel and chromel wires) that are used to form K-type thermocouple junction. The sensor is fabricated by spot welding four alumel and four chromel wires at the desired points to shape the grid structure, creating sixteen evenly distributed sensing points (junction of both wires) known as a 4x4 grid architecture (Fig. 2). The distance between each sensing point is kept to 10 mm, so that the sensor can span the 40 mm × 40 mm cell's electrode surface. The temperature impact from one junction to another due to heat transfer via conduction or via thermo-element wires with a distance of 10 mm is calculated in the order of $10^{-4}\,\mathrm{W\,K^{-1}}$, i.e., negligible.

Alumina paste is applied at the contact points between the sensor and electrode surface for electrical insulation and for bonding the sensor sensing points (SSPs) (thermoelement junctions) to the cell surface, preventing any movement during handling/operation. Silver mesh with silver paste is used at both anode and cathode electrodes for current collection. The signal from cell electrode and thermal sensor is collected by NI data logging instruments (NI cDAQ 9226, UK) and transferred to a LabVIEW programme for in-situ monitoring and recorded. A Potentiostat (Solartron® 1280C) is used for performing DC measurements and polarisation, in order to electrically monitor the cell operation/outputs at required voltage levels, and correlating these to the temperature measurements.

2.2. Sensor characteristics

A recently developed multi-point thermal sensor is applied to monitor temperature distribution of an operating SOFC. Though it has a similar working principle of conventional thermocouples (that requires two thermoelements of different type per sensing point) i.e. Seebeck theory it has a key advantage of requiring a lower number of thermoelements of each type, even for the same number of sensing points. Fundamentally, some of thermo-elements are used as a common line and shared with more than one thermoelement of the other type.

This provides more sensing points by minimising the required thermo-elements. The obtained voltage (V_{emf}) junctions are independent from each other due to the law of intermediate conductors [38]. According to this law, the net absolute thermoelectric power generated between two dissimilar materials is zero if there is uniform temperature. The basic structure of a junction of the multi-junction sensor is demonstrated in Fig. 1(a) which illustrates the technical explanation of the sensor. T_0 is assumed as the known terminal temperature (temperature at the data logger) while T_1 and T_2 are the unknown temperature that can be calculated from the resultant voltages between a-f and a-e respectively. T_0 is considered as the temperature near the data logger even though the external wire connections are made at the cell surface. This has been deemed a valid assumption since the attached external wires are selected from the same corresponding thermo-elements materials to eliminate parasitic voltage contribution at the connection.

Technically, there is no effect from the inserted thermo-element from b and c between T_0 and T_2, as long as the temperatures are the same at points b and c, in which the distance between these two points is less than 0.2 mm. Therefore, the temperature difference between
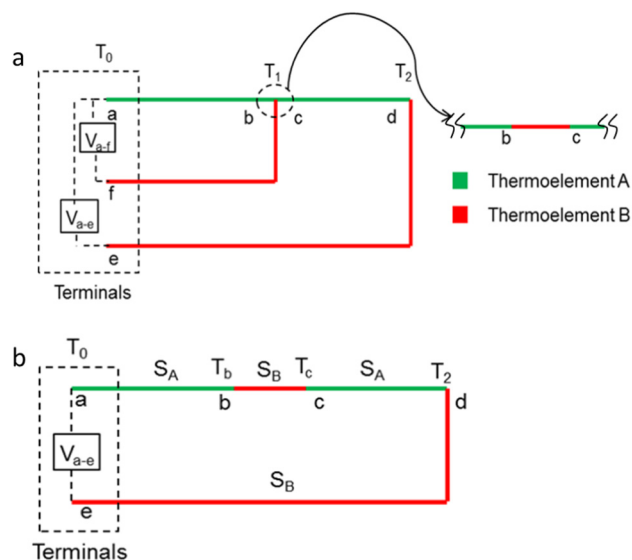
Fig. 1. (a) Basic building block of multi-junction array and (b) exaggerated view of the intermediate junction.

these two points is assumed negligible. The array structure is shown in Fig. 1(b) which is where the exaggerated view of the junction is presented with the materials Seebeck coefficient S_A, S_B and temperatures at inserted junction T_b and T_c. Without inserting b-c the architecture is a basic conventional TC block. Eqs. (1) and (2) show that there is no impact on the obtained Seebeck voltage when another thermo-element is joined to the thermocouple junction in terms of thermoelectric's of the given thermal pairs.

$$V_{emf} = \int_{T0}^{T_b} S_A dT + \int_{T_b}^{T_c} S_B dT + \int_{T_c}^{T2} S_A dT + \int_{T2}^{T0} S_B dT \tag{1}$$

where $V_{emf(a-e)}$ is the Seebeck potential between point "a" and "e" while "S_A" and "S_B" are the Seebeck coefficients for the related materials.

When the temperature for $T_b = T_c$ then the resultant Seebeck voltage is found as:

$$V_{emf} = \int_{T0}^{T2} S_A dT + \int_{T2}^{T0} S_B dT \quad V_{emf} = \int_{T0}^{T2} (S_A - S_B) dT \tag{2}$$

As seen from Fig. 1(b) and from Eq. (2) there is no impact on any other junction from the intermediate junction as long as the temperature is the same at the two sides of the added junction. Therefore, it is vital to have the junction point be as small as possible to avoid any possible thermal gradient across the junction point. In this respect, the thin-wire/thin-film sensor comes into prominence because it provides the opportunity to have an efficient junction by adjusting the techniques for joining the wires/films at the junction. The thermal mass of the thermo-elements used can be further reduced by considering its mechanical stability. As a result, the minimum thickness where the sensor can survive needs to be determined to remove any junction-related issues during operation at the harsh environment. Thickness of the used thermo-element and the position of the junction which should be perpendicular to the heat flow are vital parameters to reduce the impact of the heat transferred through the thermo-elements. If there is a considerable amount of heat transferred via these thermoelements, this can lead to a considerable error in measurement. Thus, the thin wire is used as the thermo-element for sensor fabrication in this study to minimise the error due to physical structure of the thermo-elements used. There is a good agreement found between the fabricated sensor calibration test, whereby the sensor has been calibrated by using a couple of certificated conventional thermocouple as well as with a single homemade thermal pair. A numerical analysis has also been performed and

the factors in play included changes in Seebeck coefficient and temperature gradient at the junction (Tb and Tc) which causes a thermal gradient along the multi array junction; the results proved that there is a negligible temperature error (0.07 °C) at the junction when a similar zone (where Seebeck coefficient and thermal gradient (between Tb and Tc) are negligible) has been achieved.

3. Experimental preparation (set up) and operating conditions

Fig. 2(a) shows the image of fabricated *multi-point thermal sensor* with sixteen sensing points, while Fig. 2(b) shows the location of the placed sensor sensing points (SSPs), TCs, current collector together with fuel/air inlet and outlets. Fig. 2(b) shows the schematic of the locations of the placed sensor sensing points (SSPs), TCs, current collector together with fuel/air inlet and outlets. One of the TC (TC1) is placed near S13 (sensing points 13) while the other (TC2) is located near S1. A deliberate plus-shaped silver current collector, covering approximately $3\ cm^2$ active area, is located at the center of the cell. The inlets and outlets are located on the corner of the manifold for both fuel and air (represented in Fig. 2(b)).

The schematic diagram of the main set up (Fig. 2(c)) consists of an electrochemical testing unit (1280C Potentiostat) to run the system in a desired electrochemical condition, a data logging system for both sensor and cell potential signal collection, high temperature furnace to heat the cell to its operating temperature (up to 800 °C), flow control and gas supply systems to supply required fuel and air with required flow rate and a computer to run all the control interfaces for temperature sensing, electrochemical measurements and gas flow.

During the experiment, different operating conditions including flow rates, drawn current, and furnace set temperature are applied to observe their contribution to the temperature increment. Both experiments were performed with the same set of parameters. Cell temperature average increment (CTA) and cell temperature gradient (CTG) were monitored at different operating temperatures such as 700 °C, 750 °C and 800 °C with varying flow rates and loading conditions. The CTA is calculated by taking the arithmetic average of all reading from sixteen sensing points while the difference between maximum and minimum reading among sixteen readings is taken for the calculation of CTG.

The flow rate was changed from 50 mL min^{-1} to 150 mL min^{-1} and the amount of drawn current was varied by changing the set voltage between 0.2 V and 0.8 V.

4. Results

4.1. Operating temperature effect

Fig. 3(a) shows the CTA over the set operating temperatures, and CTG along the entire cell, and experimentally-obtained OCV (OCV$_{expr}$) under constant 50 mL min^{-1} fuel flow rate at 700 °C, 750 °C and 800 °C. The OCV$_{theor}$ is computed by applying the Nernst equation shown in Eq. (1) as 1.14 V for 700 °C, 1.13 V for 750 °C, and 1.12 V for 800 °C, slightly higher than the corresponding obtained OCV$_{expr}$ (Fig. 3(c)). An obtained decrease in OCV$_{theor}$ with the increase in operating temperature is expected from Eq. (3) as a result of the inverse relation between Gibbs free energy and temperature [39]:

$$E_{nernst} = E° + \frac{RT}{nF}\ln\left[\frac{PH2 + PO2}{PH2O}\right] \tag{3}$$

As seen from Fig. 3(a), OCV$_{expr}$ decreases while CTA and the corresponding CTG increase even under OCV conditions when temperature is increased. There are two possibilities that this increase can be attributed to: (i) anodic oxidation reactions provided any remaining oxygen exists; and (ii) hydrogen direct oxidation reaction (HDOR) due to fuel crossover from anode to cathode. (ii) is the more likely case, as a higher increment is observed on the outer side of the cell.
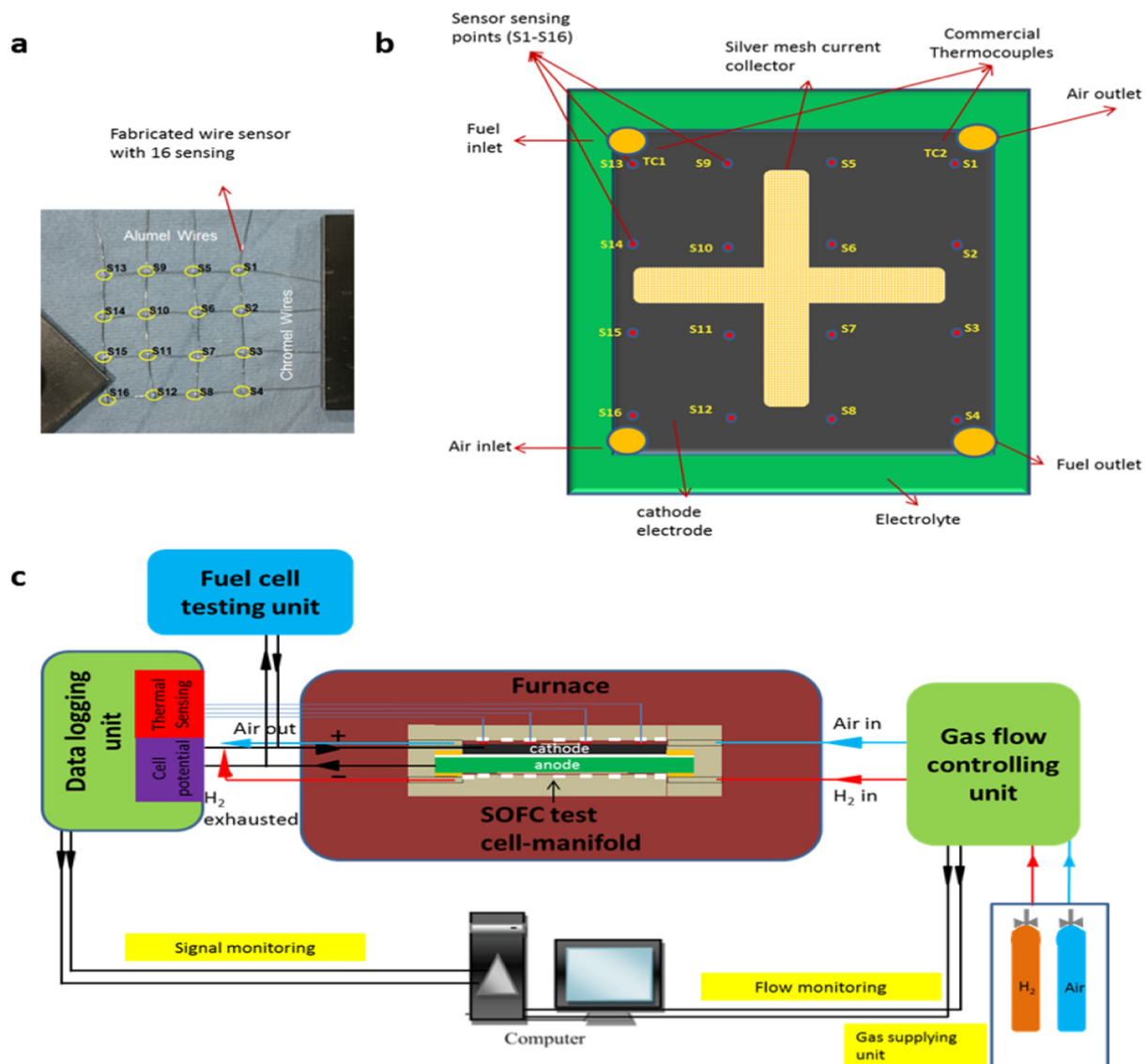
Fig. 2. (a) fabricated wired sensor with sixteen sensing points, and (b), schematic view of the sensor integrated cell-manifold configuration, and (c), the schematic diagram of the whole experimental set up (not to scale).

The increments in CTA are obtained as 1.70 °C, 3.14 °C, and 4.27 °C while CTG is observed as 0.77, 0.85, and 0.96 at the operating temperatures of 700 °C, 750 °C, and 800 °C, respectively (Fig. 3(a)). However, there are slight changes (~0.1 °C) monitored in the CTG with the varying operating temperature, signalling that the location of the heat sources which lead to cell temperature increase are similarly affected by the variation in operating temperature.

The partial pressure of H_2 increases with increasing operating temperature due to the ideal gas law which stipulates that the system pressure increases (hence partial pressure of the gas components also increase) due to increasing the temperature when the volume and provided fuel flow rate are kept the same, resulting in higher gas crossover, as given by Eq. (4) [40].

$$PV = nR\Delta T \tag{4}$$

where P is the pressure, V is the volume, n is the molar ratio, R is the gas constant and ΔT is the temperature difference.

In addition to greater pressure, the chemical and electrochemical activities of gases (H_2) are more facile with increasing temperature. This most likely reflects the contribution of the HDOR that is enhanced with increasing temperature.

Fig. 3(b) shows the 3D surface mapping of the cell electrode at

different operating temperatures. Before the reduction process, the monitored temperature is the furnace set temperature since there is no increment. However, when the reduction process is completed, there is an increment in CTA with the produced fuel, depending on the operating temperature during OCV where the maximum increment (~6 °C) is obtained at 800 °C near the fuel inlets. A high temperature is monitored at close proximity to the fuel and air inlets for all temperature sets, which is where the fuel is least depleted with higher partial pressure. Additionally, the inner side of the cell shows the lowest temperature for almost all cases, indicative that leakage is occurring from the outer side of the cell via the gasket (Thermiculite® 866).

4.2. Fuel rate effects

Fig. 4(a) and (c) show the increment in CTA, CTG and OCV variation with varying flow rate at constant operating temperature. The axis and corresponding curve is in the same colour; for instance, the green axis is for voltage changes and the line with green circle symbols represents it. The furnace operating temperature is selected as 750 °C (average temperature) and it is kept constant during the measurement. As seen from Fig. 4(a) and (c), OCV_{expr} and OCV_{theor} increased with increasing fuel
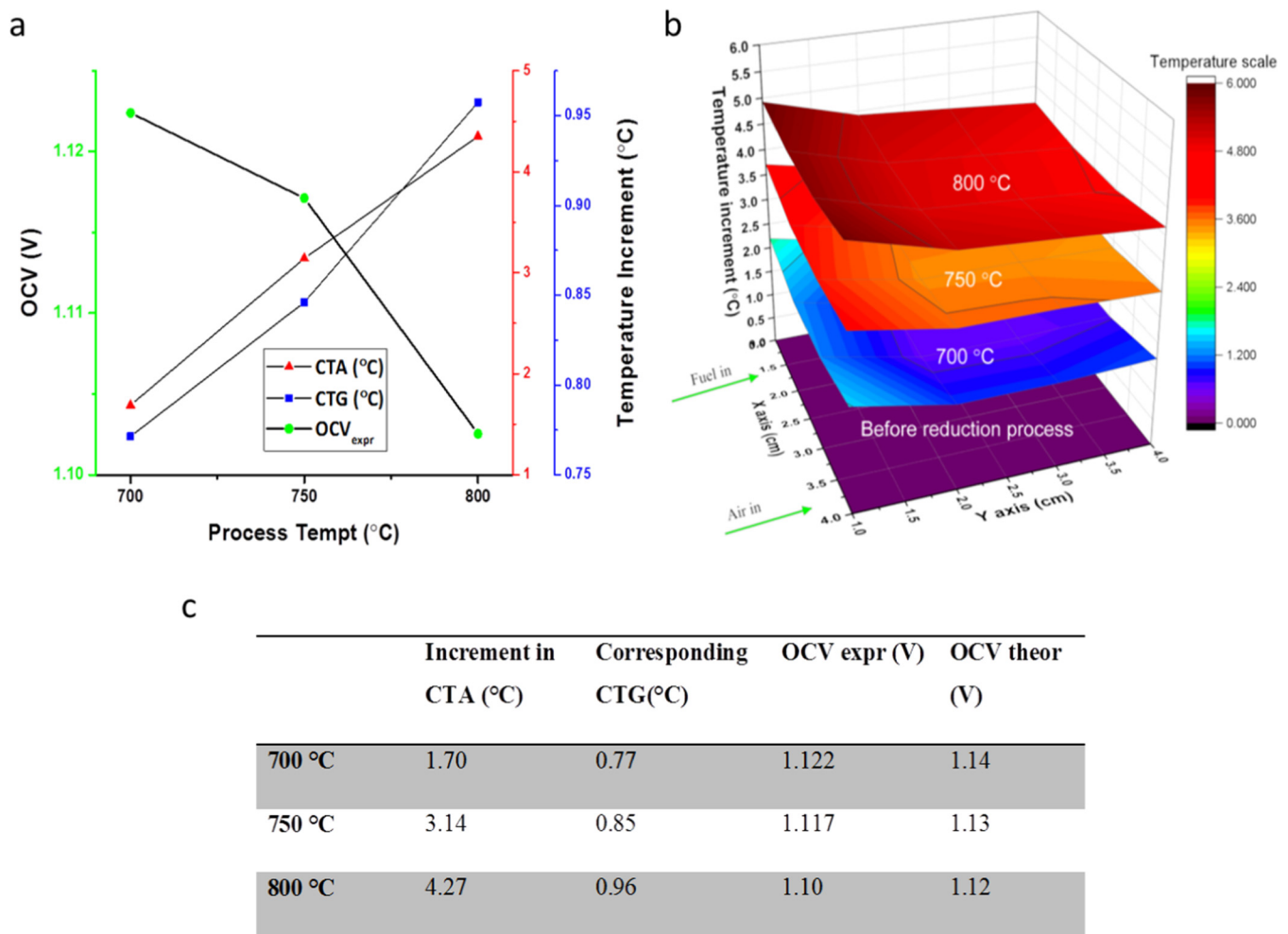
Fig. 3. (a) OCVexpr, CTG and increment in CTA at varying operating temperature with 50 mL min^{-1} constant flow rate, and (b) temperature distribution at different conditions, and (c) the table of numerical values with OCVexpr, CTG, CTA, and OCV$_{theor}$.

flow rate as a result of the increase in partial pressure of the reactants due to the relation given in the Nernst Eq. (3).

However, the CTA is also increasing together with OCV$_{expr}$, which is not expected according to the thermodynamics of SOFCs as there is an inverse relation between Gibbs free energy and operating temperature. Thus, this is attributed to unwanted direct oxidation of H_2 with O_2 due to H_2 leakage from the anode to cathode which leads to fuel crossover losses (see Eq. (5)) [39].

The equation shows that the net voltage can be obtained after deducting the losses/polarisations, including η_{act} (due to activation), η_{conc} (due to concentration), η_{ohm} (due to ohmic), and η_{fuel} (due to fuel crossover). When H_2 crosses over to the cathode through the electrolyte or via sealing, HDOR can occur with the existing oxygen due to the presence of the catalyst. The reaction is yielding no current, hence this leads to undesired heat resulting in fuel wastage at both the anode and cathode [39].

$$OCV_{expr} = OCV_{theor} - Total\ lossess\,(\eta_{act} + \eta_{conc} + \eta_{ohm} + \eta_{fuel}) \qquad (5)$$

CTA is increased by about 1.1 °C when the flow rate is doubled from 50 mL min^{-1} to 100 mL min^{-1} and 0.6 °C when a further 50% increase is incurred from 100 mL min^{-1} to 150 mL min^{-1}. The changes monitored in CTG are negligibly small with varying fuel flow rate, where increases of 0.1 °C and 0.2 °C were observed when fuel flow rate increases from 50 mL min^{-1} to 100 mL min^{-1} and from 100 mL min^{-1} to 150 mL min^{-1}, respectively (Fig. 4(c)).

The temperature profile due to fuel flow rate contribution is similar to the profile obtained with the contribution of operation temperature as shown in Fig. 4(b). For both cases, there is a greater increment observed nearby the fuel/air inlet side, while the lowest increment obtained is in the inner side of the cell. Even though the parameters are different, the reason behind their contribution is evaluated to be fuel leakage. The increase in flow rate leads to a rise in partial pressure of reactants resulting in relatively more HDOR due to higher amounts of gas leakage.

4.3. Loading effect

The variations in CTA and CTG are monitored under OCV at two different loads with a flow rate of 100 mL min^{-1} as plotted in Fig. 5(a). The furnace temperature is set to be constant (750 °C) during the measurement process.

The numerical values for the obtained CTA and CTG are shown in Fig. 5(c) at OCV, 0.8 V and 0.2 V. The CTA and CTG have shown a similar trend with varying fuel flow rate and operating temperature under OCV conditions as analysed in the previous section. However, there is a reverse relationship observed between CTA and CTG when the system changes from OCV to the constant 0.8 V loading condition. The CTA increases slightly by 0.2 °C while the CTG decreases by 0.5 °C. When the system is loaded there is heat produced due to more exothermic reactions taking place at the inner side of the cell, where the lowest temperature has been recorded during OCV condition, resulting in a relative thermal balance across the cell surface (Fig. 5(b)). Consequently, there is a decrease in CTG. Whereas, when more current is
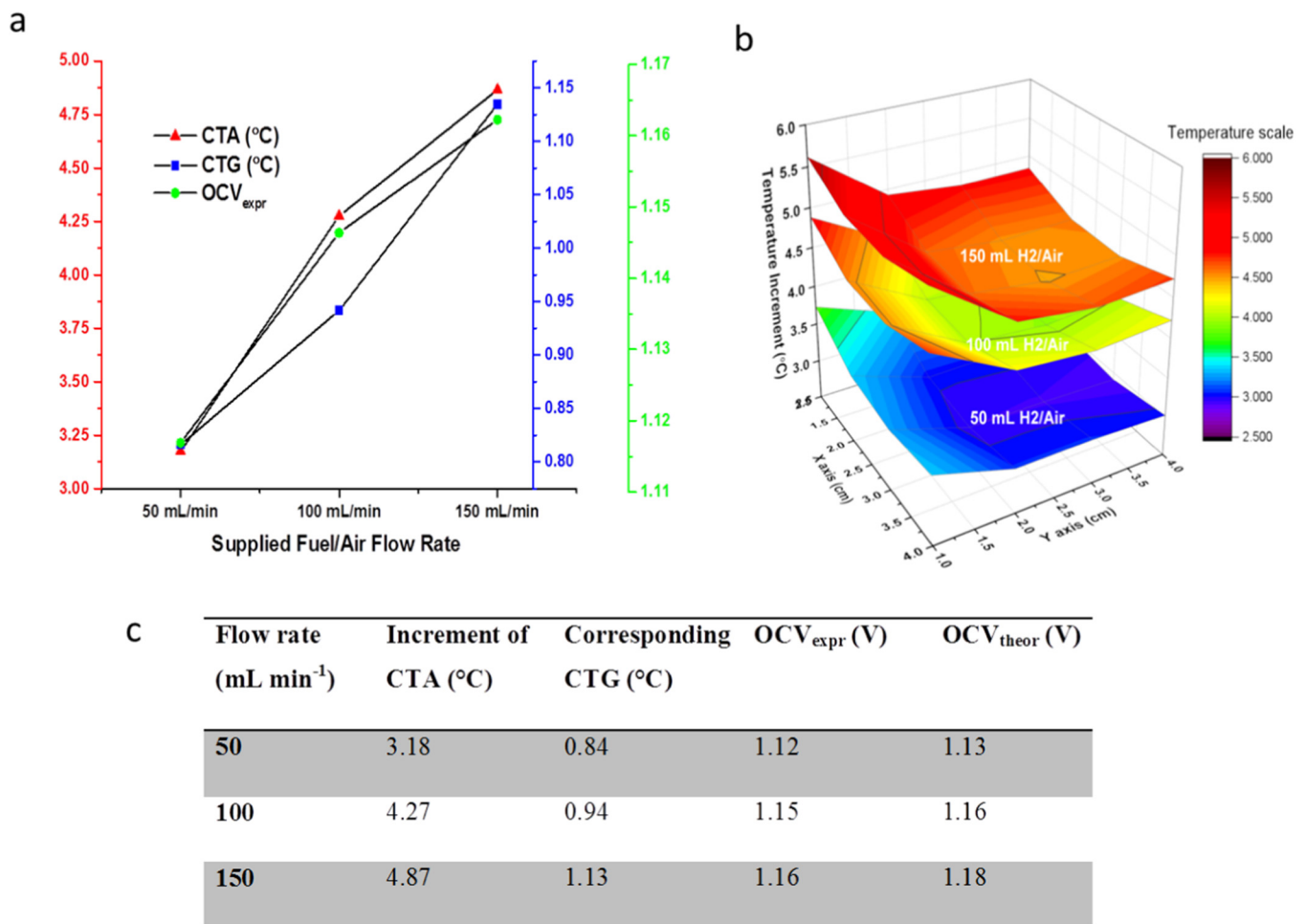
a

b

c

Flow rate (mL min⁻¹)	Increment of CTA (°C)	Corresponding CTG (°C)	OCV$_{expr}$ (V)	OCV$_{theor}$ (V)
50	3.18	0.84	1.12	1.13
100	4.27	0.94	1.15	1.16
150	4.87	1.13	1.16	1.18

Fig. 4. (a) CTA and CTG with OCV under varying flow rate, and (b) temperature distribution at different flow rate, and (c) the table of numerical values of CTA, CTG, OCV$_{expr}$, and OCV$_{theor}$.

drawn from the system at 0.2 V constant voltage, the CTG increased sharply together with the CTA from about 0.75 °C to 1.35 °C (80% change) and from about 4.5 °C to 5.55 °C (22% change), respectively. This is due to greater variation in the exothermic reactions taking place at the inner side and outer side of the cell. The surface temperature distribution of the electrode under OCV and two different loading conditions is presented in Fig. 5(b). The highest temperature increment is obtained at the inner side of the cell whilst the lowest temperature is obtained around the fuel outlet at 0.2 V.

When the system reaches thermal balance after the voltage is set to 0.2 V, the CTG is about 1.3 °C and the cell temperature increment is increased to about 1.5 °C with loading at 100 mL min⁻¹ fuel flow rate, while the temperature rise at the inner side is obtained as 2 °C. The reason for this relatively higher temperature change at the inner side of the cell is due to the cell area which is occupied by current collection, since the inner side of the cell is the location where the two axes of the plus-shaped current collector are intersecting, resulting in the bulk concentration of electrons. This addresses the importance of even distribution of the current collection mechanism. Therefore, the contact points (or contact area) of the current collector is found to be the most critical location that a temperature-induced hard (or irreversible) failure, such as cell cracks or delamination between layers, may occur. Identification of the location(s) where more heat is released is key for taking the necessary actions to remove unwanted heat from the system to minimise thermal gradients.

5. Discussions

5.1. Thermodynamic analysis of operating temperature and supplied fuel rate related temperature increment

As aforementioned, the reasons for the unexpected increase in cell temperature are attributed to the HDOR due to H_2 crossover from anode to cathode throughout the electrolyte/sealing [39]. As a result, exothermic HDOR occurs when the leaked H_2 meets with O_2 in the presence of catalysts. Eventually, heat is released leading to the temperature rise over the operating temperature even under OCV conditions. The key parameter to determine the impact of the heat released by HDOR on the cell temperature is the molar ratio ($\dot{n}_{H2}$) of leaked H_2 and its leak rate with varying flow rate. Herein, the corresponding enthalpy of the oxidation reaction (Eq. (6)) at operating temperature is applied to calculate the amount of leaked H_2. The released heat rate is the product of the leaked flow rate with the corresponding enthalpy (Eq. (7)) [41].

$$\Delta H°_{f_{H_2O,T}} = \Delta H°_{f_{H_2O,298}} + \int_{298}^{T} C_p dT \qquad (6)$$

$$\dot{Q}_{in} = \Delta H \times \dot{n}H_2 \qquad (7)$$

where $\Delta H°_{f_{H_2O,T}}$ is the reaction enthalpy at operating temperature $\Delta H°_{f_{H_2O,298}}$, is the enthalpy at room temperature, T is the operating temperature, C_p is the heat capacity, and $\dot{Q}_{in}$ is the heat rate generated due to direct oxidation of leaked H_2.

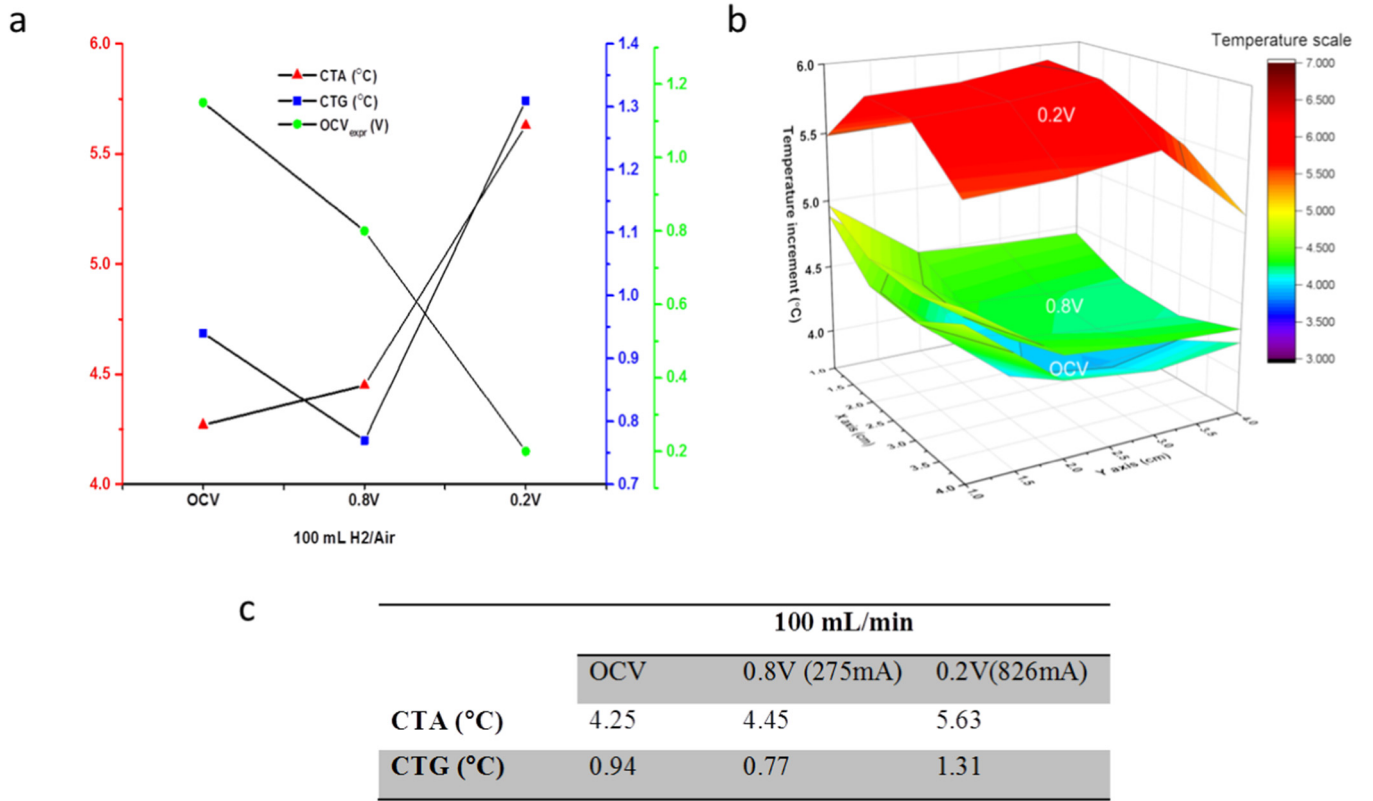The relationship between the net heat, generated heat rate and

Fig. 5. (a) Cell temperature increment with resulted gradient with corresponding voltage, (b) temperature profile of the cell under OCV and loading conditions, and (c) the table of their numerical values.

simultaneous heat loss rate is given in Eq. (8).

$$\Delta Q = \int_{t1}^{t2} \dot{Q}_{in} \, dt - \int_{t1}^{t2} \dot{Q}_{out} \, dt \, (Q_{conv}) \tag{8}$$

$$\Delta Q = Q_{cell} + Q_{manifold} \tag{9}$$

$$Q_{cell} = Q_a + Q_c + Q_{el} \text{ and } Q_i = m_i c p_i \Delta T$$

$$Q_{conv} = hA\Delta T \tag{10}$$

where ΔQ is the heat observed by the corresponding thermal mass including cell components and manifolds (Eq. (9)). These terms are separated in Eq. (8) due to their varying thermo-physical properties. $\dot{Q}_{conv}$ (Eq. (10)) is the heat flux removed by the excess gas (air at the cathode and N_2 and H_2 at the anode flow) from the cell electrode surface via convection heat transfer, Q_{conv} in which h (calculated as $h = 6.5 \, \mathrm{W \, m^{-2} \, K^{-1}}$, is the heat transfer coefficient and A is the surface area across which the heat transfer is occurring. Q_i (Eq. (9)) is the heat consumed by related components of the cell testing unit, where "a" denotes the anode, "c" denotes the cathode and "el" denotes the electrolyte, m_i (gr) is the total weight for all the involved components that the heat is transferred through and c_i ($0.6 \, \mathrm{J \, g^{-1} \, K^{-1}}$) is the heat capacity for each involved component. ΔT is the average net temperature increment which is taken from the related experimental results (Fig. 4(a)).

The leaked H_2 amount is calculated by taking the total temperature changes ($\Delta T = 0.75 \, ^\circ C$) when the fuel flow rate is increased from $50 \, \mathrm{mL \, min^{-1}}$ to $100 \, \mathrm{mL \, min^{-1}}$ for a specific time period. The time required for the given temperature rise to reasonably reach an equilibrium is monitored as ~ 1000–$1250 \, s$ (Fig. 6). Eventually, the leaked H_2 is calculated as $1.31 \times 10^{-6} \, \mathrm{mol \, s^{-1}}$ which is negligible compared to the supplied H_2 ($37 \times 10^{-3} \, \mathrm{mol \, s^{-1}}$).

Once the amount of leaked H_2 is calculated under the condition of $100 \, \mathrm{mL \, min^{-1}}$ at $750 \, ^\circ C$, the possible leakage of H_2 can be analytically simulated by writing the relationship between leakage flow and
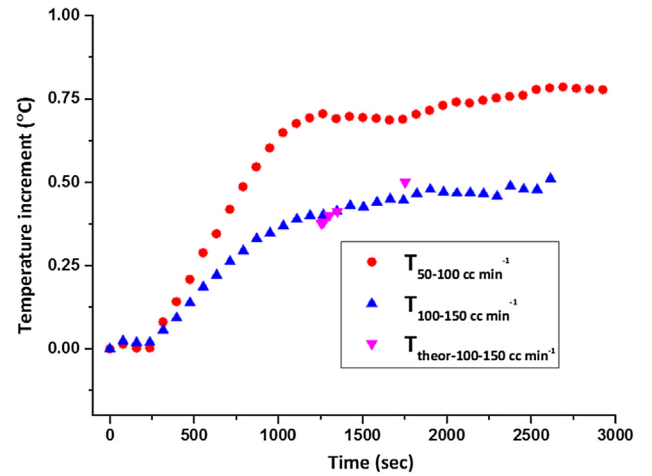

Fig. 6. Analytically and experimentally calculated temperature increment.

pressure (Eq. (11)) for varying fuel flow rate. Due to the increasing fuel flow rate the partial pressure of H_2 is increased which leads to higher leakage and finally results in a higher temperature increment.

$$\frac{F1}{F2} = \frac{h1}{h2} \tag{11}$$

where $F1$ and $F2$ are the leakage flow rates at pressures $h1$ and $h2$, respectively. Temperature increment is then calculated when the fuel flow rate increased from $100 \, \mathrm{mL \, min^{-1}}$ (0.57 atm (calculated partial pressure)) to $150 \, \mathrm{mL \, min^{-1}}$ (0.65 atm (calculated partial pressure)) by obtaining the corresponding leaked fuel amounts due to partial pressure changes. There is a good agreement observed between the experimentally- and analytically-obtained temperature increments as shown in Fig. 6. The possible temperature increment is also found for

50 mL min^{-1} as 1.8 °C as it has the highest partial pressure changes (~0.4 atm) compared to the changes when the fuel is increased from 50 mL min^{-1} to 100 mL min^{-1} (~0.17 atm changes) and 100 mL min^{-1} to 150 mL min^{-1} (~0.08 atm). Thus, if the increment due to fuel leakage is subtracted from the total increment (3.28 °C see Fig. 4(a)) obtained with 50 mL min^{-1}, the impact of the electrochemical activities related to this temperature increment occurring during the anode reduction is found as 1.5 °C.

5.2. Thermodynamic analysis of loading correlated temperature increment

When a system reaches an equilibrium condition, it is assumed that the heat released by the cell and the heat lost to the environment is equal. The heat transfer via conduction to the other parts of the system such as manifold, gasket and mesh used for current collection is completed which helps to determine the thermal mass absorbs the released heat. The released heat from these electrochemical reactions is calculated by using Eq. (12) with the assumption that the electrochemical reaction is taking place at the infinitely thin layer [42].

$$Q_e = R_e \times \Delta H - I \times E_{cell} \tag{12}$$

where Q_e is the released electrochemical heat, R_e is the reaction rate based on H_2 molar consumption and ΔH is the reaction enthalpy while I is the current and E_{cell} is the cell operating potential.

Using the given flow rate of air, the molar flow of oxygen is calculated by assuming the air is an ideal gas (Eq. (13)). The corresponding H_2 (Re) which reacts with the transferred oxygen at the anode can be computed by using the reaction stoichiometry.

$$n = \frac{VP}{RT} = \frac{1 \text{ atm} \times 40 \text{ mL/min}}{(0.08206 \text{ L} \times \text{atm} \times \text{mol}^{-1} \times \text{K}^{-1})(1027 \text{ K})} \tag{13}$$

where n is the molar ratio, P is the pressure, V is the flow rate T is the operating temperature and R is the gas constant.

Alternatively the molar flow of H_2 as a reactant of the oxidation reaction can also be computed by using the drawn current (with corresponding cell voltage) via Eq. (14) [39].

$$Re = mA\left(\frac{C}{s}\right) \times \frac{1 \text{ mol e}-}{96485 \text{ C}} \times \frac{1 \text{ mol H2}}{2 \text{ mol e}-} \tag{14}$$

Following which, obtaining/calculating the required parameters including E_{cell}, I, R_e and ΔH from the experimental findings and conditions, the released heat (Q_e) is calculated. For the heat loss via convection the same parameters used in the previous section are still applicable where the heat convection coefficient was calculated as $h = 6.5 \text{ W m}^{-2}\text{K}^{-1}$.

The theoretical temperature rise is calculated for a period of ~600 s, which is the time taken for the system to reach a reasonable equilibrium condition, and this rise is compared with the experimentally-obtained increment as presented in Fig. 7. There is good agreement observed between the analytically-obtained and experimental measured temperature rise over the given time frame. Beyond this time (600 s), the increment rate is negligible, e.g. from 600 s to 800 s, where there is no considerable change monitored as shown in Fig. 7.

As presented in Fig. 5(b) the higher temperature increment is monitored on the inner side of the electrode where the current collector is placed. In the literature, the temperature profile of the cell surface is shaped depending on fuel flow direction/types [25,43,44]. It is usual that larger temperature increments are obtained in the vicinity of the fuel/air inlet which is ascribed to the higher rate of fuel utilisation. However, in this study the effect observed from the fuel direction is almost negligible compared to the effect when there is non-uniformity in current collection. Hence, from the experience of this study, the importance of the interconnect design and its contact mechanisms is brought to the fore. It is identified as a key parameter to understand/minimise the cell temperature gradient as it is challenging to provide uniform electrical connection between cell electrodes and interconnect
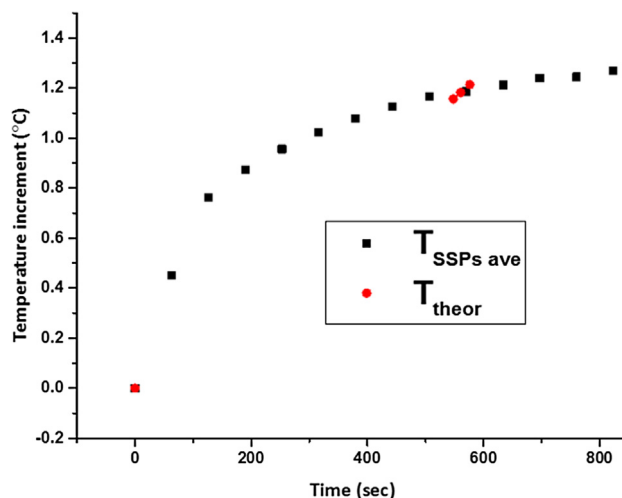

Fig. 7. Experimentally and analytically obtained temperature increment by time.

across the cell entire cell surface.

In the case of drawing 826 mA (0.2 V) with 100 mL min^{-1} of fuel/air flow rate at fixed furnace temperature (750 °C), the overall temperature rise is found as 5.75 °C. Table 1 shows the percentage of the parameters' contribution to the obtained temperature increment out of the overall increment, by assessing the proportion of their individual contributions. The highest contribution is observed from the unexpected gas/charge crossover-related temperature increment with 45%. The temperature increase percentage from electrochemical reactions (28%) and anode reduction process reactions (27%) are comparable. Since the current drawn is limited due to the small-sized collection area (only 20% of the total electrode active area covered for current collection), the increment from the cells electrochemical activity can be further increased by expanding the size of the current collection area. By ignoring the increment (taken as a reference point and calculating the changes beyond this) due to the anode reduction process, the rate of the contribution of the fuel leakage and drawn current to CTG is also calculated (also shown in Table 1). In contrast with their contributions to CTA, there is a more severe CTG occurring when the system is loaded (40%) compared to the obtained CTG from fuel crossover (15%).

It is revealed from the results that the fuel leakage-related temperature rise is another contributor to the temperature increment together with cell activities. Moreover, even though its contribution varies depending on the experimental condition, its impact is not negligible and is worth considering as significant for SOFC thermal gradient issues. Thus, it is important to account for other heat contributors to understand the realistic relationship between the temperature increments and performance degradation or thermal stress analysis.

In this study, the non-uniform (but symmetric) current collection mechanism provides an understanding of the importance of the location and effectiveness of the connection between the electrode surface and current collector [34,45]. According to the results, the effect of the current collection mechanism location on temperature distribution is more dominant than the previously discussed parameters, including fuel/air effects, flow rate and leakage effects. The importance of the current collection mechanism on cell performance degradation has already been expressed in the literature [46], while its impact on cell temperature distribution has not been studied fully yet. Investigation of the impact of current collection mechanism on the temperature distribution might provide key understanding for performance degradation pertaining to rib detachment (or fuel/air distribution whilst proper current distribution is achieved) of a cell by monitoring its temperature profile [47]. These are all directly related to the current density (cell power output [6]) variation which is distributed depending on the

Table 1
Parameters and their impact on total temperature increment (5.5 °C).

	Heat source/sink	Location	Contribution to CTA	Contribution to CTG
Anode reduction	Source	Anode	27%	Reference point
Unexpected crossover (fuel or electrons)	Source	Cathode	45%	15%
Electrochemical reaction	Source	Anode and cathode	28%	40%

current collection mechanism since, as soon as the electrons reach the cathode, they possibly start reacting more through the depth of the cathode rather than horizontally spreading through the placed current collector. Subsequently, the electrochemical reactions take place around the first contact point more than any other side of the electrode, possibly also contributing to higher increment observed at the inner side of the cell, where the electrical connection is made in this study. Thus, the even distribution of collection mechanism is vital for minimising the thermal gradient and therefore a sensitive temperature sensing platform is paramount in evaluating the effectiveness of the collection mechanism. In other words, the impact of fuel utilisation on temperature gradient is strongly dependent on the effectiveness of the current collection mechanism in terms of electrical uniformity. The study has also pointed out the difficulty in distinguishing the individual impact of these parameters on SOFC temperature distribution using conventional TC-based measurements.

6. Conclusions

The contributions of some key parameters including operating temperature, fuel flow rate, and electrochemical reactions to SOFC average temperature and temperature gradient are monitored in-situ. Additionally, the findings are analytically calculated based on the SOFCs' thermodynamics. There is a temperature increment experienced with varying operating set temperature even with a constant fuel flow rate. The temperature increment is higher near to the fuel/air inlet which gradually decreases through to the fuel outlet. It is ascribed to the higher possibility of the occurrence of H_2 leakages near the inlet due to relatively higher partial pressure at the inlet leading to more direct oxidation and resulting in higher heat release. With the increase in temperature, this makes the gas components more active and leads to an increased pressure. These both contribute to the gas leakages resulting in more direct oxidation and corresponding temperature increments. The temperature increment was also observed with the increasing flow rate under the same set/operating temperature which was also attributed to undesired fuel crossover through the electrolyte resulting in direct H_2 oxidation. This can be either oxygen ions (reduced at cathode due to free electrons or the electron crossover) travelling from cathode to anode or H_2 from anode to cathode eventually leading to an exothermic reaction between O_2 and H_2 resulting in heat release to the atmosphere. According to the obtained temperature increment, the released heat and its corresponding required reactant (fuel) were calculated.

Cell electrode temperature increment due to electrochemical cell reactions and its impact on corresponding temperature distribution were monitored during loading conditions with varying drawn currents at constant furnace temperature and fuel flow rate. Experimentally obtained heat is compared with the analytically calculated value under steady state conditions. The analytical obtained increment matches well with the experimentally measured increment. The percentage of the contribution of each individual value on the increment of the cell temperature out of the total obtained increment is computed. The direct oxidation was found as the most dominant parameter on temperature increment while the electrochemical reactions have the highest impact on temperature distribution.

The obtained value of the temperature increment can vary depending on the experimental conditions; however the characteristics of the temperature profile and time dependency to reach reasonable equilibrium for each action remains relatively constant. There are two key points to identify the source for the temperature increment experienced during SOFC operation: (i) the location where the increments are monitored and (ii) how quick these increments occur. For instance, if there is higher temperature appearing near the inlet this not likely down to fuel utilisation, instead gas leakage may be the reason/contributor for the increment. Additionally, if there is a sudden increase observed on the inner side of a cell this is then most likely being caused by electrochemical reactions. This shows the benefits provided by the high temporal (sudden increase) and spatial resolutions (temperature profile) of the implemented sensor.

Acknowledgement

References

[1] Bae K, Jang DY, Choi HJ, Kim D, Hong J, Kim BK, et al. Demonstrating the potential of yttrium-doped barium zirconate electrolyte for high-performance fuel cells. Nat Commun 2017;8:1–9.

[2] Graves C, Ebbesen SD, Jensen SH, Simonsen SB, Mogensen MB. Eliminating degradation in solid oxide electrochemical cells by reversible operation. Nat Mater 2015;14(2):239–44.

[3] Chen Y, Yang L, Ren F, An K. Visualizing the structural evolution of LSM/xYSZ composite cathodes for SOFC by in-situ neutron diffraction. Sci Rep 2014;4.

[4] Xu H, Chen B, Tan P, Cai W, He W, Farrusseng D, et al. Modeling of all porous solid oxide fuel cells. Appl Energy 2018;219(February):105–13.

[5] Oryshchyn D, Harun NF, Tucker D, Bryden KM, Shadle L. Fuel utilization effects on system efficiency in solid oxide fuel cell gas turbine hybrid systems. Appl Energy 2018;228(July):1953–65.

[6] Lim DK, Im HN, Song SJ. Spatial distribution of oxygen chemical potential under potential gradients and theoretical maximum power density with 8YSZ electrolyte. Sci Rep 2016;6(November 2015):6–11.

[7] Wang K, Hissel D, Péra MC, Steiner N, Marra D, Sorrentino M, et al. A review on solid oxide fuel cell models. Int J Hydrogen Energy Jun. 2011;36(12):7212–28.

[8] Minh NQ. Solid oxide fuel cell technology - features and applications. Solid State Ionics 2004;174(1–4):271–7.

[9] M. Andersson and B. Sunden, "Technology Review – Solid Oxide Fuel Cell," Stockholm, 2017.

[10] Yan D, Zhang C, Liang L, Li K, Jia L, Pu J, et al. Degradation analysis and durability improvement for SOFC 1-cell stack. Appl Energy 2016.

[11] Sandhu NK, Hanifi AR, Woldnik A, Amiri T, Etsell TH, Luo J, et al. Electrochemical performance of a short tubular solid oxide fuel cell stack at intermediate temperatures. Appl Energy 2016;183:358–68.

[12] Vijay P, Hosseini S, Tadé MO. A novel concept for improved thermal management of the planar SOFC. Chem Eng Res Des 2013;91(3):560–72.

[13] Zaccaria V, Tucker D, Traverso A. A distributed real-time model of degradation in a solid oxide fuel cell, part II: analysis of fuel cell performance and potential failures. J Power Sources 2016;327:736–42.

[14] Zhu J, Lin Z. Degradations of the electrochemical performance of solid oxide fuel cell induced by material microstructure evolutions. Appl Energy 2018;231(April):22–8.

[15] Baldinelli A, Barelli L, Bidini G, Di Michele A, Vivani R. SOFC direct fuelling with high-methane gases: optimal strategies for fuel dilution and upgrade to avoid quick degradation. Energy Convers Manag 2016;124:492–503.

[16] Zhang Z, Li S, Xiao Y, Yang Y. Intelligent simultaneous fault diagnosis for solid oxide fuel cell system based on deep learning. Appl Energy 2019;233–234(August 2018):930–42.

[17] Mizusawa T, Araki T, Mori M. Temperature and reactive current distributions in

microtubular solid oxide electrolysis cells. Int J Hydrogen Energy 2016;41(32):13888–900.

[18] Lang M, Bohn C, Henke M, Schiller G, Willich C, Hauler F. Understanding the current-voltage behavior of high temperature solid oxide fuel cell stacks. J Electrochem Soc 2017;164(13):F1460–70.

[19] Mafra L, Pascual MJ, Kharton VV, Tsipis EV. Thermal and mechanical stability of lanthanide- containing glass – ceramic sealants for solid oxide," no. i; 2014. p. 1834–46.

[20] Schlegl H, Dawson R. Finite element analysis and modelling of thermal stress in solid oxide fuel cells. Proc Inst Mech Eng Part A J Power Energy 2017;231(7):654–65.

[21] Aydın Ö, Nakajima H, Kitahara T. Reliability of the numerical SOFC models for estimating the spatial current and temperature variations. Int J Hydrogen Energy 2016;41(34):15311–24.

[22] Xenos DP, Hofmann P, Panopoulos KD, Kakaras E. Detailed transient thermal si-mulation of a planar SOFC (solid oxide fuel cell) using gPROMS™. Energy 2015;81:84–102.

[23] Wei T, Huang Y-H, Zeng R, Yuan L-X, Hu X-L, Zhang W-X, et al. Evaluation of Ca3Co2O6 as cathode material for high-performance solid-oxide fuel cell. Sci Rep 2013;3(1):1125.

[24] Doppler MC, Fleig J, Bram M, Opitz AK. Hydrogen oxidation mechanisms on Ni/yttria stabilized zirconia anodes: Separation of reaction pathways by geometry variation of pattern electrodes. J Power Sources 2018;380(October 2017):46–54.

[25] Fardadi M, McLarty DF, Jabbari F. Investigation of thermal control for different SOFC flow geometries. Appl Energy 2016;178:43–55.

[26] Barelli L, Bidini G, Cinti G, Ottaviano a. SOFC regulation at constant temperature: experimental test and data regression study. Energy Convers Manag 2016;117:289–96.

[27] Xu M, Li TS, Yang M, Andersson M, Fransson I, Larsson T, et al. Modeling of an anode supported solid oxide fuel cell focusing on thermal stresses. Int J Hydrogen Energy 2016;41(33):14927–40.

[28] Pianko-Oprych P, Zinko T, Jaworski Z. A numerical investigation of the thermal stresses of a planar solid oxide fuel cell. Materials (Basel) 2016;9(10):814.

[29] Robinson JB, Brown LD, Jervis R, Taiwo OO, Heenan TMM, Millichamp J, et al. Investigating the effect of thermal gradients on stress in solid oxide fuel cell anodes using combined synchrotron radiation and thermal imaging. J Power Sources 2015;288:473–81.

[30] Chiang L-K, Liu H-C, Shiu Y-H, Lee C-H, Lee R-Y. Thermal stress and thermo-elec-trochemical analysis of a planar anode-supported solid oxide fuel cell: effects of anode porosity. J Power Sources 2010;195(7):1895–904.

[31] Son JW, Song HS. Influence of current collector and cathode area discrepancy on performance evaluation of solid oxide fuel cell with thin-film-processed cathode. Int J Precis Eng Manuf - Green Technol 2014;1(4):313–6.

[32] Li T, Wu Z, Li K. A dual-structured anode/Ni-mesh current collector hollow fibre for micro-tubular solid oxide fuel cells (SOFCs). J Power Sources

2014;251(Apr):145–51.

[33] Guo Y, Liu Y, Cai R, Chen D, Ran R, Shao Z. Electrochemical contribution of silver current collector to oxygen reduction reaction over Ba0.5Sr0.5Co0.8Fe0.2O3 − δ electrode on oxygen-ionic conducting electrolyte. Int J Hydrogen Energy 2012;37(19):14492–500.

[34] Rolle A, Thoréton V, Rozier P, Capoen E, Mentré O, Boukamp B, et al. Evidence of the current collector effect: study of the SOFC cathode material Ca 3 Co 4 O 9 + δ. Fuel Cells 2012;12(2):288–301.

[35] Guk E, Kim J-S, Ranaweera M, Venkatesan V, Jackson L. In-situ monitoring of temperature distribution in operating solid oxide fuel cell cathode using proprietary sensory techniques versus commercial thermocouples. Appl Energy 2018;230(August):551–62.

[36] Guk E, Ranaweera M, Venkatesan V, Kim JS. Performance and durability of thin film thermocouple array on a porous electrode. Sensors (Switzerland) 2016;16(9):1–2.

[37] Fluri A, Pergolesi D, Roddatis V, Wokaun A, Lippert T. In situ stress observation in oxide films and how tensile stress influences oxygen ion conduction. Nat Commun 2016;7:1–9.

[38] Pollock DD. The theory and properties of thermocouple elements, Philadelphia; 2015.

[39] Kaur G. Solid oxide fuel cell components: interfacial compatibility of SOFC glass seals. Solid oxide fuel cell components: interfacial compatibility of SOFC glass seals. 2015. p. 1–408.

[40] Park JM, Kim DY, Baek JD, Yoon Y, Su P, Lee SH. Effect of electrolyte thickness on electrochemical reactions and thermo-fluidic characteristics inside a SOFC Unit Cell; 2018.

[41] Aydın Ö, Nakajima H, Kitahara T. Processes involving in the temperature variations in solid oxide fuel cells in-situ analyzed through electrode-segmentation method. J Electrochem Soc 2016;163(3):F216–24.

[42] Ho TX, Kosinski P, Hoffmann AC, Vik A. Effects of heat sources on the performance of a planar solid oxide fuel cell. Int J Hydrogen Energy 2010;35(9):4276–84.

[43] Fan P, Li G, Zeng Y, Zhang X. Numerical study on thermal stresses of a planar solid oxide fuel cell. Int J Therm Sci 2014;77(Mar.):1–10.

[44] Al-Masri A, Peksen M, Blum L, Stolten D. A 3D CFD model for predicting the temperature distribution in a full scale APU SOFC short stack under transient op-erating conditions. Appl Energy 2014;135(Dec.):539–47.

[45] Channa K, De Silva R, Kaseman BJ, Bayless DJ. Silver (Ag) as anode and cathode current collectors in high temperature planar solid oxide fuel cells. Int J Hydrogen Energy 2011;36(1):779–86.

[46] Kuhn M, Napporn TW, Meunier M, Therriault D. Experimental study of current collection in single-chamber micro solid oxide fuel cells with comblike electrodes. J Electrochem Soc 2008;155(10):B994.

[47] Barelli L, Barluzzi E, Bidini G. Diagnosis methodology and technique for solid oxide fuel cells: a review. Int J Hydrogen Energy 2013;38(12):5060–74.